

The multi-scale dynamics of all-optical exchange bias reversal

Floris J. F. van Riel,^{a)} Andries B. M. Droste, Bert Koopmans, and Diana C. Leitaó
*Department of Applied Physics, Eindhoven University of Technology, P.O. Box 513, 5600 MB Eindhoven,
 The Netherlands*

(Dated: 20 February 2026)

Pinning magnetization in a ferromagnetic thin film is commonly realized through exchange biasing with an adjacent antiferromagnet. Field-cooling from above the Néel temperature is a reliable yet slow re-pinning method in exchange-biased systems. For on-demand reprogrammable devices, localized and rapid exchange bias repinning methods are essential. Recent work has shown that femtosecond laser pulses enable field-free reversal of exchange bias in tailored multilayer stacks. Contrary to field-cooling, our experiments with ultrafast excitation reach hitherto unexplored regimes in the exchange bias setting process. Here, we unravel these observations by considering both ultrafast magnetization dynamics on the femto- to picosecond timescale and slow heat-driven dynamics on millisecond timescales and upwards. We develop a microscopic framework of exchange bias setting in a polycrystalline antiferromagnetic thin film like IrMn that provides a complete description of the observations in our present experiments and those found in literature. We expand the use of our model by identifying material platforms and stack designs that lead to optimized performance, aiding further development of optically reprogrammable devices.

I. INTRODUCTION

In spintronics devices, exchange bias is frequently used as a robust magnetic pinning mechanism that induces a preferential magnetization orientation at a ferromagnetic/antiferromagnetic interface¹. This phenomenon enables stable referencing solutions, e.g., for magnetic sensors² or memory devices³. Iridium-manganese alloys $\text{Ir}_x\text{Mn}_{1-x}$ are a type of antiferromagnet that is commonly used in sputter-deposited thin film stacks for exchange biasing transition-metal ferromagnetic systems⁴⁻⁹. When depositing IrMn on a ferromagnetic layer, its magnetic configuration will be imprinted in the IrMn, imposing an effective unidirectional exchange bias field H_{EB} on the ferromagnet via exchange coupling with the Mn spins at the interface^{10,11}. After deposition, manipulation of the exchange bias may be realized by field-cooling through the Néel temperature, either globally by thermal annealing or locally through Joule heating¹²⁻¹⁴ or laser heating¹⁵⁻¹⁷.

These annealing methods rely on an externally applied magnetic field to guide the setting of H_{EB} . However, recent research has shown the possibility of field-free and ultrafast manipulation of exchange bias by all-optical magnetization switching with femtosecond laser pulses¹⁸⁻²⁰. Exchange bias reversal with single-shot laser pulses was first observed in thin film stacks containing antiferromagnetic IrMn and Co-Gd ferrimagnetic alloys¹⁹ or multilayers²⁰. In our recent study²⁰, we showed how specifically tailored thin film stacks experience a full 180° reversal of H_{EB} from up to down and vice versa upon excitation by a single laser pulse. Even though the reversal effect itself is evident, our present results also indicate a creep-like evolution of the magnitude of H_{EB} across

several days that hitherto remained unexplored. Particularly, grasping the complete picture of the underlying mechanism is challenged by the complexity of the setting process occurring because of the ultrafast heating and the highly non-equilibrium states governing the dynamics, but these processes are critical for determining the long-term pinning stability in devices.

In this work, we show how a mixture of ultrafast excitation and slow temperature relaxation can explain the creep of H_{EB} and how future applied research may leverage these concepts for optimized performance in reprogrammable devices. We present a model based on previous works²¹⁻²⁴ that in all its simplicity produces very rich and unexpected results when combined with ultrafast magnetization switching. A wide range of timescales (from 10^{-15} to 10^{17} s) is considered to explain observations from present experiments and reveal the multi-scale dynamics of all-optical exchange bias reversal. The outcomes provide guidelines for future research on designing and fabricating laser-reprogrammable exchange-biased devices.

II. EXPERIMENTAL DEMONSTRATION

The creep-like evolution of H_{EB} was observed in thin film stacks from our recent study²⁰ $\text{Ta}(4)/\text{Pt}(4)/\text{Co}(0.6)/\text{Gd}(5.5)/\text{Co}(1)/[\text{Pt}(1.25)/\text{Co}(0.6)]_{x2}/\text{Ir}_{20}\text{Mn}_{80}(4)/\text{Ta}(4)$ (thicknesses in nm) grown by magnetron sputtering on a thermally oxidized Si/SiO₂ wafer. On these stacks, we measure the magnetic response to excitation by a ~ 100 fs linearly polarized laser pulse with a Gaussian spatial energy profile and a central wavelength of 700 nm. Hysteresis loops were measured by *ex-situ* Kerr microscopy of the illuminated sample area. The measurement was performed once directly after excitation at $t_{\text{meas}} = 0$ days and then a second time after approximately $t_{\text{meas}} = 100$ days, at which

^{a)}f.j.f.v.riel@tue.nl

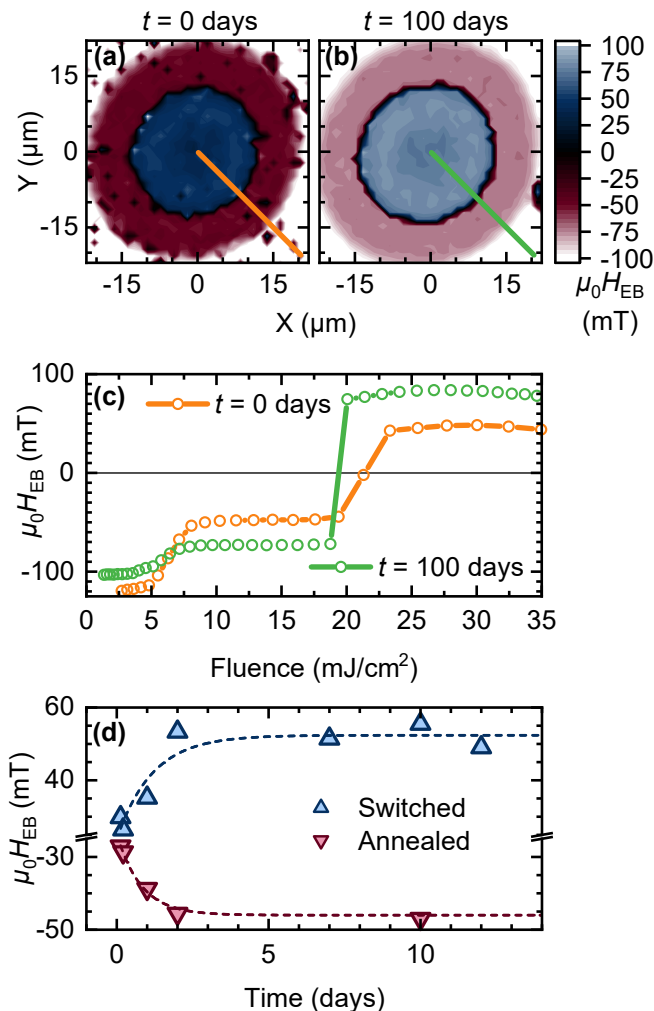


FIG. 1. (a) Experimentally measured map of the exchange bias field magnitude H_{EB} across a region of the sample that was illuminated by a single femtosecond Gaussian laser spot with a peak fluence of 38 mJ cm^{-2} . The measurement is performed by Kerr microscopy field sweeps directly after laser excitation, where H_{EB} is locally extracted from the hysteresis curve field shift. (b) The same measurement as in (a) but performed 100 days after illumination. (c) Radial cross-sections of the distribution of H_{EB} as indicated by the orange and green lines in (a) and (b). (d) A demonstration of the evolution of H_{EB} from a newly deposited and switched sample over the period of two weeks, for both the annealed (red) and switched (blue) regions from (a). The dashed lines are guides to the eye.

point a significantly different magnitude of H_{EB} is measured, which is shown in Fig. 1. Figure 1a shows the top-down processed microscopy image from the initial measurement and Fig. 1b shows the measurement after 100 days, with blue and red colors indicating positive and negative values of H_{EB} . The Gaussian fluence (energy per area) profile of the laser pulse is reflected in the circularly symmetric profile of H_{EB} . The color map reveals three general regions: unaffected for low fluences

(white), affected but not switched (annealed) for medium fluences (red) and switched for high fluences (blue). By comparing the colors between Fig. 1a and Fig. 1b it is evident that the profile of the annealed/switched regions is identical, but the absolute values of H_{EB} have increased in both regions. The orange and green lines are cross-sections of the profile that are plotted in Fig. 1c. Similar trends of H_{EB} evolving over several days at room temperature have been reported previously by Migliorini et al.²⁵ for polycrystalline IrMn films, where it is also speculated that direct exchange between spins at the ferromagnetic/antiferromagnetic interface drives the setting process.

We also studied the time-dependence of H_{EB} on the timescale of days and found that both the annealed and switched regions evolve with approximately the same timescale, as shown in Fig. 1d. To capture the complete picture we formulated a model²⁰ that extends the magnetization dynamics beyond the ultrafast regime. We identified thermally assisted relaxation of antiferromagnetic grains as the primary mechanism for explaining the slow creep-like evolution of H_{EB} . Below we elaborate on the extended models for both the ultrafast and slow magnetization dynamics and how they are linked together to describe the full exchange bias reversal process from excitation to relaxation.

III. MODELING THE REVERSAL PROCESS

In order for our model to predict the behavior of the exchange bias upon ultrafast excitation, it first needs to predict the outcome of the magnetization switching in the ferrimagnet for a given laser fluence P_0 . This is achieved using the layered microscopic three temperature model (M3TM)^{26,27}, which models magnetization dynamics on the femtosecond to picosecond timescale. We model our stacks by the layered system shown in Fig. 2a. Here, a ‘layer’ is an atomically thin entity with an associated normalized magnetization $m_z = M_z/M(T = 0 \text{ K})$ along the perpendicular z -axis, arising from the spins of the electrons. We consider a stack with perpendicular magnetic anisotropy so only the z -component of m is non-zero, i.e. $m = m_z$. Magnetic exchange interaction between atoms – both within and between layers – is captured by an exchange splitting energy Δ_i separating spin energy levels, given by Eq. A1 and schematically illustrated in Fig. 2b. We use spin quantum numbers $S_{\text{Co}} = S_{\text{Mn}} = 1/2$ and $S_{\text{Gd}} = 7/2$ for the respective Co, Mn and Gd atoms²⁸.

The laser heat gets distributed over two thermodynamic systems: electrons directly absorb the laser light and transfer it to phonons via electron-phonon scattering. Both electron and phonon systems are given an associated temperature T_e and T_p , respectively, which are coupled via Eq. A4. Figure 2c shows the evolution of T_e and T_p as a function of time after laser excitation, where the excitation itself occurs at time $t = 0$ and is annotated by the roman numeral (i) in Fig. 2d. The magneti-

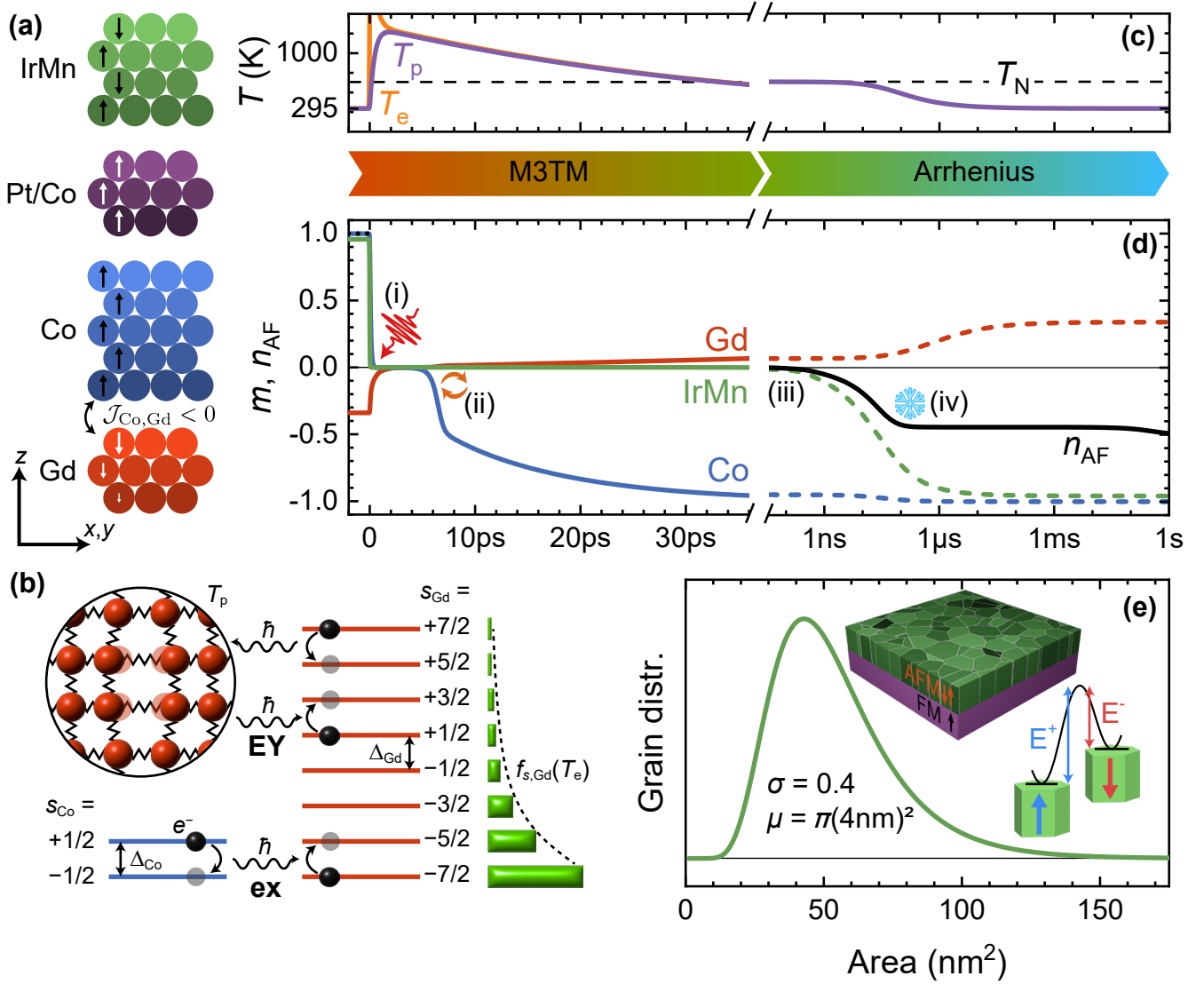


FIG. 2. (a) Overview of the simulated stack, consisting of in total 15 atomic monolayers of Gd, Co, Pt/Co (modeled as a single compound ferromagnet) and IrMn (modeled as a layered antiferromagnet). The symbol \mathcal{J}_{ij} represents the exchange coupling between atoms of species i and j . (b) Schematic of the processes modeled by the M3TM framework, exemplified for Gd and Co. The lines represent the energy levels for the various spin quantum numbers s_i which are spaced by the exchange splitting Δ_i . On top is shown the Elliot-Yafet (EY) spin-flip scattering by creation/annihilation of a phonon and on the bottom is shown the exchange scattering (ex) between two electrons exchanging angular momentum. The green bars on the right represent the occupation fraction $f_{s,Gd}$ of each spin level in Gd in equilibrium. (c) The evolution of temperature T over time for illumination by a $58.3 \times 10^8 \text{ J m}^{-3}$ laser pulse, also taking into account the difference between the electron (T_e) and phonon (T_p) temperatures within the first picosecond after excitation. The dashed line represents the Néel temperature T_N . (d) Evolution of the layer-averaged magnetization m in the Gd (red), Co (blue) and IrMn (green) subsystems, alongside the exchange bias parameter n_{AF} . The dotted line before 0 and the dashed lines after ~ 36 ps represent their respective values in thermal equilibrium. Above the plot is indicated which modeling framework – M3TM or Arrhenius – is used in each temporal regime. Four key events are highlighted in roman numerals: (i) laser incidence, (ii) ferromagnetic reversal and remagnetization, (iii) T dropping below T_N and antiferromagnetic remagnetization and (iv) freezing in of the exchange bias. (e) Plot of the log-normally distributed areas of the grains, with parameters μ and σ as used in Eq. B4. The inset illustrates how the Arrhenius law is applied to the antiferromagnet (AFM). When the ferromagnet (FM) is uniformly magnetized up, the grains that contribute positively to the exchange bias have a lower energy than grains that contribute negatively. The energy required for a grain to spontaneously transition from up to down (down to up) is indicated by E^+ (E^-).

zation reversal is driven by Elliot-Yafet electron-phonon spin-flip scattering and by electron-electron angular momentum exchange scattering, as schematically shown in Fig. 2b. Both Elliot-Yafet and exchange scattering processes depend on T_e and/or T_p following Eq. A6. Figure 2d shows how the magnetization m evolves over time for a fluence $P_0 = 58.3 \times 10^5 \text{ mJ cm}^{-3}$ above the switching threshold, noting that the synthetic ferrimagnet Co/Gd remagnetizes in the opposite direction when the temperature drops below the Curie temperature, as annotated with (ii) in Fig. 2d. Details on implementation of the M3TM are given in Appendix A.

The outcome of the M3TM is binary, i.e. it can only predict whether or not reversal of the exchange bias takes place by looking at the magnetic state (up or down) of the Pt/Co system after remagnetization. At this time after excitation, ultrafast processes no longer play a significant role. In this regime, we approximate the system temperature as $T = T_e = T_p$ and we assume the magnetization in all layers is equal to its equilibrium value at temperature T according to Eq. A5. In order to now predict the exchange bias magnitude, we simulate the magnetic state of the antiferromagnet in more detail.

The polycrystalline antiferromagnet is modeled as a collection of non-interacting columnar grains with a fixed distribution (median area μ and standard deviation σ , see Fig. 2e). Note that when we refer to the grain area, we mean the area A of a particular grain from the distribution and not the median area μ of the whole distribution. All grains are subject to heat-driven transitions between states separated by an energy barrier. Because of the ultrafast excitation and subsequent rapid cooling, it is expected that grains are excited far out of their thermal equilibrium state and may become trapped in metastable states once the energy barriers exceed the thermal energy required to overcome them. These processes become leading as soon as the temperature drops below the magnetic ordering temperature of the antiferromagnet, that is the Néel temperature T_N , annotated in Fig. 2d with (iii).

Transitions under the influence of thermal energy are modeled using Arrhenius' law. Transitions in the ferromagnet may be neglected due to the large intralayer exchange coupling that is much stronger than the interlayer exchange bias coupling. For simplicity, each grain either contributes positively (\uparrow) or negatively (\downarrow) to the total H_{EB} . We label the fraction of grains with area A that contribute positively (negatively) to H_{EB} as n^\uparrow (n^\downarrow), and the timescale for spontaneously switching from \uparrow to \downarrow (\downarrow to \uparrow) as $\tau_{\downarrow\uparrow}$ ($\tau_{\uparrow\downarrow}$).

Arrhenius' law dictates that these timescales are proportional to the exponential of an energy barrier (see Fig. 2e). We will assume that the energy landscape of each antiferromagnetic grain is determined by a uniaxial perpendicular anisotropy and by a unidirectional exchange coupling across the interface with the adjacent ferromagnet. The anisotropy energy density is given by $K_{AF} = K_{AF,0} m_i^2$ and the exchange energy per unit area

by $\mathcal{J}_{ex} = \mathcal{J}_{ex,0} m_i m_j$, where m_i and m_j are the antiferromagnetic and ferromagnetic equilibrium magnetization according to Eq. A5, respectively. We use $K_{AF,0} = 5.56 \times 10^5 \text{ J m}^{-3}$ for IrMn²³ and an area-dependent $\mathcal{J}_{ex,0}$ as explained in Supplementary Section 1²⁹⁻³¹. We note that the sign of \mathcal{J}_{ex} is determined by the signs of m_i and m_j . Combining all this into expressions for the transition times we get^{32,33}

$$\tau_{\downarrow\uparrow} = \tau_0 \exp(E^+/k_B T), \quad (1a)$$

$$\tau_{\uparrow\downarrow} = \tau_0 \exp(E^-/k_B T), \quad (1b)$$

$$E^\pm = A \begin{cases} K_{AF} t_{AF} \pm \mathcal{J}_{ex} + \mathcal{J}_{ex}^2/4K_{AF} t_{AF} & \text{if } |\mathcal{J}_{ex}| < 2K_{AF} t_{AF} \\ \max(0, \pm 2\mathcal{J}_{ex}) & \text{if } |\mathcal{J}_{ex}| > 2K_{AF} t_{AF} \end{cases},$$

where $\tau_0 \sim 10^{-10} \text{ s}$ is the attempt time. Note that the transition times in Eqs. 1 are strongly dependent on T (also through $m_{i,j}$), the grain area A and the antiferromagnetic thickness t_{AF} .

To quantify the grain alignment, we define the parameter $n_{AF} \equiv n^\uparrow - n^\downarrow$ which takes values in the range $[-1, 1]$, where a value of +1 (-1) means all grains with area A contribute positively (negatively) to H_{EB} . From Arrhenius' law, an ordinary differential rate equation governing the evolution of n_{AF} can be derived, and is given by

$$\frac{dn_{AF}}{dt} = \left(\frac{1}{\tau_{\downarrow\uparrow}} - \frac{1}{\tau_{\uparrow\downarrow}} \right) \left[1 - n_{AF} \coth \left(\frac{\mathcal{J}_{ex} A}{k_B T} \right) \right]. \quad (2)$$

This equation may be solved for all areas A and then integrated over the entire distribution to find the magnitude h_{EB} of exchange bias according to Eq. B3. This value is normalized to the maximal attainable exchange bias $H_{EB,max}$ for an infinitely thick antiferromagnet at $T = 0 \text{ K}$, that is $h_{EB} = H_{EB}/H_{EB,max}$. Equation 2 has a stable solution in thermal equilibrium that is equal to $n_{AF} = \tanh(\mathcal{J}_{ex} A/k_B T)$. The approximate time it takes to reach this value is also known from Eq. 2 to be $\sim (1/\tau_{\downarrow\uparrow} - 1/\tau_{\uparrow\downarrow})^{-1}$, with $T = T_{amb}$. Note that for $t_{AF} = 10 \text{ nm}$ it only takes a grain of modest 50 nm^2 area for this time to exceed the age of the universe ($4.3 \times 10^{17} \text{ s}$). Therefore, all but the smallest grains will never reach full equilibrium after laser excitation, but rather they stall at some intermediate value between $n_{AF} = 0$ and thermal equilibrium. This is exemplified by the black line in Fig. 2d which halts its evolution after T drops below a certain freezing point ((iv) in Fig. 2d). More details and equations from this part of the model are found in Appendix B.

IV. MODEL RESULTS AND DISCUSSION

We now use our model to investigate the temporal evolution of individual grains and look at parametric dependencies. For $P_0 = 58.3 \times 10^8 \text{ J m}^{-3}$ and $t_{AF} = 5 \text{ nm}$,

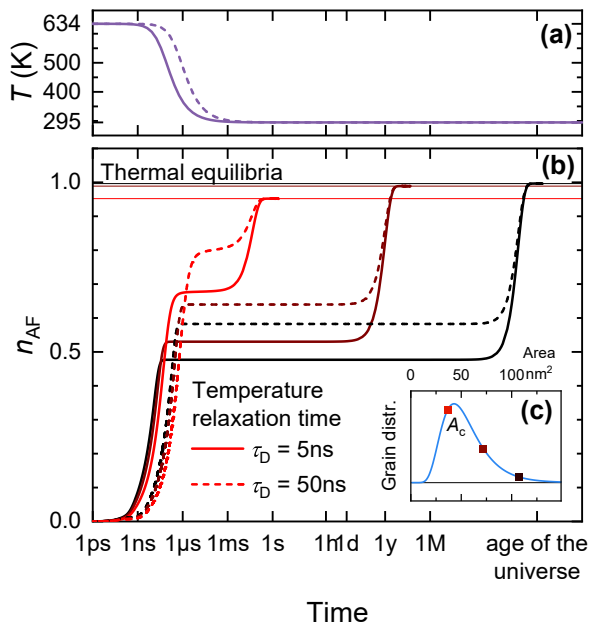


FIG. 3. (a) The temperature T after laser excitation according to Eq. B1 for $\tau_D = 5$ ns (solid line) and $\tau_D = 50$ ns (dashed line). Time is measured from the moment that T drops below the Néel temperature $T_N = 634$ K of IrMn. (b) Solutions to Eq. 2 of the parameter n_{AF} for three different grain sizes (see the inset (c) for a distribution of the grain areas and the sampling of the three grain sizes). The smallest grain (red) is taken to be the critical grain area A_c for an antiferromagnet that is $t_{AF} = 5$ nm thick. The solid lines are simulated for a temperature relaxation time of $\tau_D = 5$ ns which is typical for the stacks used in the experiment. The dashed lines are simulated for an artificial but achievable value of $\tau_D = 50$ ns. The solid horizontal lines at the top of (b) are the steady-state solutions of Eq. 2 that represent thermal equilibrium.

the temporal evolution of T and n_{AF} obtained by solving Eq. 2 is shown for three different grain areas in Figs. 3a and 3b. The three grain areas are drawn from the log-normal distribution plotted in Fig. 2e with typical values $\mu = \pi(8\text{ nm})^2$ and $\sigma = 0.4^{23}$. The smallest area is chosen to be equal to the critical grain area A_c from Eq. B2, below which grains are superparamagnetic and do not contribute to exchange bias. As is evident from Fig. 3, we may distinguish two stages in the setting process: once halting at some intermediate level when T drops below the freezing point and once when reaching thermal equilibrium. For each of the three grain sizes the intermediate level after freezing is slightly different, with smaller grains reaching higher intermediate values of n_{AF} . Moreover, the timescale at which the level is reached is slightly shorter for larger grains. Crucially however, the smaller grains reach thermal equilibrium orders of magnitude earlier than the larger grains. This explains the creep-like evolution of exchange bias observed in our experiments from Fig. 1.

It is also shown in Fig. 3 that artificially slowing down

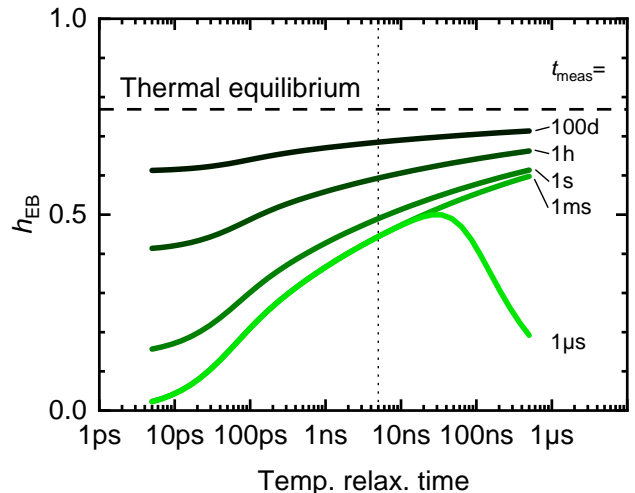


FIG. 4. The normalized value of the exchange bias field h_{EB} reached at various time points t_{meas} after excitation, plotted as a function of the temperature relaxation timescale τ_D . The values are found by integrating the state of n_{AF} from the plots in Fig. 3 over the entire grain size distribution. The values are normalized to the maximum attainable value $H_{EB,max}$ corresponding to the limiting case of an infinitely thick antiferromagnet at $T = 0$ K. The vertical dotted line corresponds to the expected value $\tau_D = 5$ ns for our stacks. The horizontal dashed line is the thermal equilibrium value of h_{EB} at room temperature according to Eq. B5.

the temperature cooling helps improve the freezing value of n_{AF} . The cooling time is determined by the temperature relaxation time τ_D , which enters the model through Eq. B1 and is mostly determined by the stack configuration. The solid lines in Fig. 3 correspond to a typical value for our stacks of $\tau_D = 5$ ns, while the dashed lines correspond to a slower relaxation time $\tau_D = 50$ ns. It can be seen that for all grains, the freezing value of n_{AF} is improved by increasing τ_D , even though the time needed to reach thermal equilibrium is not significantly changed.

To make this more quantitative, we simulate the outcome of h_{EB} for different values of τ_D and for different measurement times t_{meas} . Figure 4 depicts the trends of h_{EB} as a function of τ_D , where $\tau_D = 5$ ns is indicated with a vertical dotted line. From Fig. 4 we can learn three important things. Firstly, the benefits of a longer τ_D are always present, but are most pronounced for shorter t_{meas} . Secondly, for very fast measurement – i.e., short t_{meas} – there is an optimal τ_D that maximizes the attainable exchange bias magnitude. Lastly, it can be seen that decreasing t_{meas} from 1 ms to 1 μs does not incur any significant losses in the reached value of h_{EB} , which is promising for applications requiring high repetition rates. In practice, manipulation of τ_D may be achieved by engineering the stack composition or geometry, for example by incorporating thermal insulators that trap the heat in the magnetic layers. Our simulations support this strategy and predict an improvement

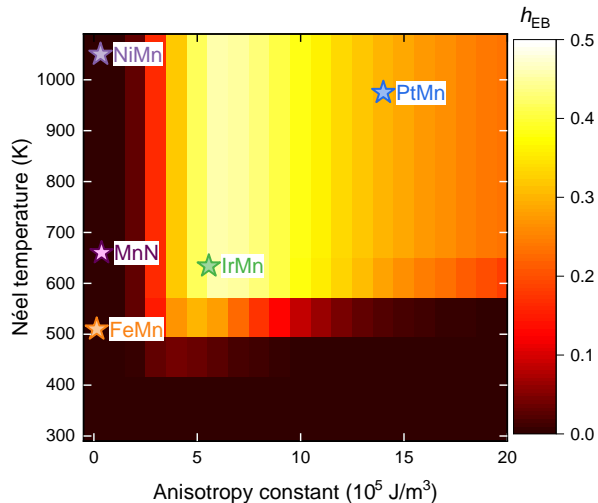


FIG. 5. The value of h_{EB} integrated over all grain areas 1 ms after laser excitation for different combinations of Néel temperature T_N and anisotropy constant $K_{AF,0}$. The stars indicate a selection of examples from real-world materials: IrMn^{23,28,34}, PtMn^{28,35}, NiMn^{28,34,35}, FeMn^{28,34} and MnN³⁶.

of ~ 10 percent points in the magnitude of the reversed exchange bias.

Other parameters besides the temperature relaxation time may also be engineered, for example by choosing a material for the antiferromagnet. Many classes of antiferromagnets exist, with a variety of different Néel temperatures and anisotropy constants. The Mn-based alloys, such as IrMn used in our experiments but also PtMn or FeMn, are conducting and therefore useful in current-perpendicular-to-plane devices like tunnel magnetoresistive sensors. Choosing the parameters T_N and K_{AF} according to values found for these materials in literature^{23,28,34–36}, we can make a reasonable guess for which material is most promising for the type of ultrafast reversal experiment we are conducting. In Fig. 5, we show a state diagram for h_{EB} after 1 ms keeping the same parameters as before but varying T_N and K_{AF} , also pointing out where various materials are expected to reside. In fact, our model predicts that IrMn occupies a sweet spot in the parameter space, having an anisotropy constant that is large enough to ensure preservation of exchange bias during the rapid temperature settling (unlike FeMn or NiMn), and small enough that it does not hinder the ability of the grains to transition to the reversed state (unlike PtMn).

One way that IrMn may be further optimized is by considering its grain size distribution. In Supplementary Section 2 we show how the value of h_{EB} after 1 ms depends on μ and σ from Eq. B4. Although these are much harder to control in experiments, it is known that grains are enlarged by annealing at high temperatures and that the buffer layer is also a contributing factor³³. It is noteworthy to see in the state diagram in Supplementary Figure 1 that there appears to be an optimal

median grain size μ and that better performance is expected for narrower distributions (i.e., lower σ) around this optimal μ . Thus, our model predicts that manipulating the grain size distribution can certainly lead to improved performance.

As a final note, we emphasize that our model can be used to describe various types of systems and experiments. To demonstrate, we performed a fluence dependency study on the stacks used by Guo et al.¹⁹, which consist of a Gd₂₃Co₇₇ ferrimagnetic alloy grown on top of IrMn. The experimental results on alloys are different from our multilayers. For example, the alloys lack the annealed plateau observed in Fig. 1c. This difference can be understood by considering the fact that the switching fluence threshold is typically larger for multilayers than for alloys²⁷. In other words: when ramping up the fluence P_0 , in our multilayer stacks T exceeds T_N before switching is achieved, while for alloys switching may be achieved before T exceeds T_N . Another difference between alloys and multilayers is that the attained value of h_{EB} is typically lower for alloys than for multilayers, which can be understood from the reduced fraction of Co-Mn pairs at the ferrimagnetic-antiferromagnetic interface and the negligible Gd-Mn coupling that does not contribute significantly to the exchange bias setting³⁷. In Supplementary Section 3 we give details on how we implemented the GdCo alloys into our model and show that it produces good correspondence between our simulated results and experimental results from Guo et al.¹⁹.

This exemplifies that for future research, the versatility of our model can prove useful for predicting the outcomes in a wide variety of situations. For example, the effect of multiple laser pulses can easily be implemented by modifying the temperature evolution in Eq. B1. Moreover, magnetization dynamics under the influence of an external magnetic field may be implemented by a coupled Landau-Lifshitz-Gilbert system.

V. CONCLUSIONS

In conclusion, we developed a model describing exchange bias reversal on both the ultrashort and long timescales. The model explains observations from field-free ultrafast laser-induced exchange bias reversal experiments, where slow creep-like evolution of the exchange bias occurred at timescales much longer than the ultrashort laser excitation. Heat-driven transitions in antiferromagnetic grains were identified as an underlying mechanism for this effect. We showed that the model is able to predict the reversal fraction and detailed temporal evolution, allowing us to identify parameters that may be tailored for optimizing the performance. In particular, we consider the temperature relaxation timescale a promising candidate and predict an improvement in the magnitude of exchange bias up to ~ 10 percent points. We also expect multilayer stacks with IrMn to outperform any other common antiferromagnetic Mn-based alloys,

although strategies with different buffer layers or additional annealing steps may be able to push the exchange bias reversal performance even further. Thus, for future research, our modeling framework guides the design and fabrication of optically reprogrammable devices.

ACKNOWLEDGMENTS

This work was financially supported by the Eindhoven Hendrik Casimir Institute.

AUTHOR CONTRIBUTIONS

F.J.F.v.R. wrote the manuscript, performed the experiments and analyzed the data, A.B.M.D. performed and analyzed the long timescale measurements, B.K. and D.C.L. supervised the work and revised the manuscript.

Appendix A: Ultrafast magnetization switching

The ultrafast part of the model is built up of N macrospin subsystems labeled $i = 1, \dots, N$ that represent, e.g., individual atomic monolayers in a multilayer thin film or a species of atoms in an alloy. Each subsystem has an associated magnetization with z -component m_i in the range $[-1, 1]$, normalized to its value at $T = 0$ K. In equilibrium, the magnetization m_i in layer i is determined by the exchange splitting Δ_i of the spin levels in the layer, i.e., the energy difference between spin levels s and $s \pm 1$. We define the matrix \mathbf{U} as

$$U_{ij} = C_{ij} \mathcal{J}_{ij} \frac{\mu_{\text{at},j}}{2\mu_B}, \quad \text{such that} \\ \Delta_i = 2\mu_B \mu_0 H + \mathbf{U} \cdot \mathbf{m}. \quad (\text{A1})$$

Here, \mathcal{J}_{ij} is the Heisenberg exchange energy between atoms in layers i and j , μ_{at} is the atomic magnetic moment, $\mu_B \approx 9.274 \text{ J T}^{-1}$ is the Bohr magneton and H is the externally applied magnetic field. For all our simulations $H = 0$, but it may also be set to any non-zero value. Assuming a (111)-oriented closely-packed lattice of atoms, we define a coordination matrix C_{ij} , which for an alloy A_xB_{1-x} of magnetic elements A and B takes the form

$$\mathbf{C} = 12 \begin{pmatrix} x & 1-x \\ x & 1-x \end{pmatrix}, \quad (\text{A2})$$

while for a multilayer it becomes the $N \times N$ matrix

$$\mathbf{C} = \begin{pmatrix} 6 & 3 & 0 & 0 & \dots \\ 3 & 6 & 3 & 0 & \dots \\ 0 & 3 & 6 & 3 & \dots \\ 0 & 0 & 3 & 6 & \dots \\ \vdots & \vdots & \vdots & \vdots & \ddots \end{pmatrix}. \quad (\text{A3})$$

Multilayers containing alloys are then easily constructed by mixing Eqs. A2 and A3 into a single coordination matrix.

The temperatures T_e and T_p are assumed to be homogeneous across all layers and evolve according to the coupled set of differential equations

$$\gamma T_e \frac{dT_e}{dt} = -g_{\text{ep}} (T_e - T_p) + \frac{P_0}{\Gamma \sqrt{\pi}} \exp\left(-\frac{t^2}{\Gamma^2}\right), \\ C_p \frac{dT_p}{dt} = g_{\text{ep}} (T_e - T_p) + C_p \frac{T_{\text{amb}} - T_p}{\tau_D}. \quad (\text{A4})$$

Here, $\gamma = 2.0 \times 10^3 \text{ J m}^{-3} \text{ K}^{-2}$ is the temperature coefficient of the electronic heat capacity, $C_p = 4 \times 10^6 \text{ J m}^{-3} \text{ K}^{-1}$ is the phonon heat capacity, $g_{\text{ep}} = 4.05 \times 10^6 \text{ J m}^{-3} \text{ K}^{-1} \text{ ps}^{-1}$ is the electron-phonon heat exchange coupling, $\Gamma = 50 \text{ fs}$ is the pulse width, $T_{\text{amb}} = 295 \text{ K}$ is the ambient temperature and τ_D is the temperature relaxation time.

An antiferromagnet is modeled in this framework as a layered ferromagnet with $\mathcal{J}_{i,i} > 0$ and $\mathcal{J}_{i,i\pm 1} < 0$. Moreover, the Zeeman splitting term in Eq. A1 is ignored for all antiferromagnetic layers.

The magnetization in equilibrium is computed using

$$m_i = -\frac{1}{S_i} \sum_{s=-S_i}^{S_i} s f_{s,i}, \quad (\text{A5}) \\ f_{s,i} = \exp\left(s \frac{\Delta_i}{k_B T_e}\right) / \sum_{s'=-S_i}^{S_i} \exp\left(s' \frac{\Delta_i}{k_B T_e}\right),$$

with $f_{s,i}$ the occupation fractions of spin level s in equilibrium following Boltzmann statistics. Equation A5 conveniently reduces to $m_i = \mathcal{B}_{S_i}(S_i \Delta_i / k_B T)$ with \mathcal{B}_S the Brillouin function for spin quantum number S . However, for a full description of the dynamics it is required to keep track of the occupation of all spin levels separately.

The equilibrium values of $f_{s,i}$ are used as the initial conditions for solving a system of ordinary differential equations that describe the evolution of $f_{s,i}$ out of equilibrium. The rate equations consist of one term accounting for Elliot-Yafet spin-flip electron-phonon scattering events (EY) and one term accounting for electron-electron scattering events with exchange of angular momentum (ex),

$$\frac{df_{s,i}}{dt} = \left. \frac{df_{s,i}}{dt} \right|_{\text{EY}}(T_p, T_e) + \left. \frac{df_{s,i}}{dt} \right|_{\text{ex}}(T_e). \quad (\text{A6})$$

The full rate equations can be found in Beens et al.²⁷.

The 'EY'-term is mostly governed by the material-dependent spin-flip probability a_{sf} . The 'ex'-term scales with an integral representing the probability that a scattering event between two electrons exchanging one unit of angular momentum with energy cost $\Delta x = (\Delta_i -$

$\Delta_j)/k_B T_e$ takes place,

$$\iiint dx_1 dx_2 dx_3 [1 - f(x_1 + x_2 + \Delta x - x_3)] \times [1 - f(x_3)] f(x_2) f(x_1) = \frac{\Delta x}{6} \frac{4\pi^2 + \Delta x^2}{1 - \exp(-\Delta x)}. \quad (\text{A7})$$

The integral in Eq. A7 was solved analytically for the Fermi-Dirac distribution function $f(x) = 1/(e^x + 1)$.

Appendix B: Exchange bias setting

In this part of the model, the evolution of n_{AF} (Eq. 2) is considered. Since the timescales are much longer than the picosecond rates in the M3TM part, the magnetization m_i in each subsystem i of the stack is assumed to be equal to its equilibrium value according to Eq. A5. The temperature is assumed to decay according to a one-dimensional heat kernel with a $t^{-1/2}$ time-dependence. Explicitly, this looks like

$$T(t) = T_{\text{amb}} + \frac{T_f - T_{\text{amb}}}{\sqrt{(t - t_0)/\tau_D} + 1}. \quad (\text{B1})$$

Here, τ_D is the temperature relaxation timescale. T_f and t_0 are parameters whose explicit formulas have been previously reported²⁰.

The critical grain size is determined by the superparamagnetic limit and is defined here as

$$A_c = 25 \frac{k_B T_{\text{amb}}}{K_{AF} t_{AF}}, \quad (\text{B2})$$

with T_{amb} the ambient temperature. For calculating H_{EB} , the value of n_{AF} is integrated over all grain sizes larger than A_c , taking the distribution function into account.

The exchange bias at time t is calculated via

$$h_{EB}(t) = \int_{A_c}^{\infty} d\mathbb{L} n_{AF}(A, t), \quad (\text{B3})$$

where $d\mathbb{L}$ is the log-normal probability density for the grain size distribution defined by

$$d\mathbb{L} = \frac{1}{A\sigma\sqrt{2\pi}} \exp\left(-\frac{\ln^2(A/\mu)}{2\sigma^2}\right) dA. \quad (\text{B4})$$

The limiting value in thermal equilibrium for a given ambient temperature T_{amb} is given by

$$h_{EB,eq} = \int_{A_c}^{\infty} d\mathbb{L} \tanh\left(\frac{\mathcal{J}_{ex} A}{k_B T_{\text{amb}}}\right), \quad (\text{B5})$$

which has been used to calculate the thermal equilibrium value in Fig. 4.

REFERENCES

- ¹B. Dieny, I. L. Prejbeanu, K. Garello, P. Gambardella, P. Freitas, R. Lehndorff, W. Raberg, U. Ebels, S. O. Demokritov, J. Akerman, A. Deac, P. Pirro, C. Adelman, A. Anane, A. V. Chumak, A. Hirohata, S. Mangin, S. O. Valenzuela, M. C. Onbaşlı, M. D'Aquino, G. Prenat, G. Finocchio, L. Lopez-Diaz, R. Chantrell, O. Chubykalo-Fesenko, and P. Bortolotti, "Opportunities and challenges for spintronics in the microelectronics industry," *Nature Electronics* **3**, 446–459 (2020), arXiv:1908.10584.
- ²D. C. Leitao, F. J. F. van Riel, M. Rasly, P. D. R. Araujo, M. Salvador, E. Paz, and B. Koopmans, "Enhanced performance and functionality in spintronic sensors," *npj Spintronics* **2**, 54 (2024).
- ³X. Guo, J. Yun, Q. Bai, Y. Zuo, and L. Xi, "Enhancement of Writing Efficiency for Multilevel Memory in Perpendicularly Magnetized Pt/Co/Pt/IrMn Multilayers," *SSRN Electronic Journal* **564** (2022), 10.2139/ssrn.4224229.
- ⁴J. Sort, V. Baltz, F. Garcia, B. Rodmacq, and B. Dieny, "Tailoring perpendicular exchange bias in [Pt/Co]-IrMn multilayers," *Physical Review B* **71**, 054411 (2005).
- ⁵J. Y. Chen, N. Thiyagarajah, H. J. Xu, and J. M. D. Coey, "Perpendicular exchange bias effect in sputter-deposited CoFe/IrMn bilayers," *Applied Physics Letters* **104**, 152405 (2014).
- ⁶J. Feng, H. F. Liu, H. X. Wei, X. G. Zhang, Y. Ren, X. Li, Y. Wang, J. P. Wang, and X. F. Han, "Giant Perpendicular Exchange Bias in a Subnanometer Inverted (Co/Pt)_n/Co/IrMn Structure," *Physical Review Applied* **7**, 1–8 (2017).
- ⁷H. Gao and Y. Liu, "Exchange bias of [Pt/Co]/IrMn with two-directional isotropy," *AIP Advances* **9**, 015132 (2019).
- ⁸X. Guo, J. Yun, Q. Bai, Y. Zuo, and L. Xi, "Enhancement of writing efficiency for multilevel memory in perpendicularly magnetized Pt/Co/Pt/IrMn multilayers," *Journal of Magnetism and Magnetic Materials* **564**, 170111 (2022).
- ⁹M. Wang, M. Li, Y. Lu, X. Xu, and Y. Jiang, "Electric field controlled perpendicular exchange bias in Ta/Pt/Co/IrMn/Pt heterostructure," *Applied Physics Letters* **123** (2023), 10.1063/5.0160957.
- ¹⁰W. H. Meiklejohn and C. P. Bean, "New Magnetic Anisotropy," *Physical Review* **102**, 1413–1414 (1956).
- ¹¹J. Nogués and I. K. Schuller, "Exchange bias," *Journal of Magnetism and Magnetic Materials* **192**, 203–232 (1999).
- ¹²J. Cao and P. P. Freitas, "Wheatstone bridge sensor composed of linear MgO magnetic tunnel junctions," *Journal of Applied Physics* **107**, 09E712 (2010).
- ¹³C. Papusoi, R. C. Sousa, B. Dieny, I. L. Prejbeanu, Y. Conraux, K. Mackay, and J. P. Nozières, "Reversing exchange bias in thermally assisted magnetic random access memory cell by electric current heating pulses," *Journal of Applied Physics* **104** (2008), 10.1063/1.2951931.
- ¹⁴W. Wang, Y. Chen, B. Wang, L. Wang, Y. Han, W. Su, Z. Hu, Z. Wang, and M. Liu, "Locally Reconfigurable Exchange Bias for Tunable Spintronics by Pulsed Current Injection," *physica status solidi (RRL) – Rapid Research Letters* **18** (2024), 10.1002/psrr.202300303.
- ¹⁵I. Berthold, U. Löschner, J. Schille, R. Ebert, and H. Exner, "Exchange Bias Realignment Using a Laser-based Direct-write Technique," *Physics Procedia* **56**, 1136–1142 (2014).
- ¹⁶M. Almeida, P. Matthes, O. Ueberschär, M. Müller, R. Ecke, H. Exner, M. Albrecht, and S. Schulz, "Optimum Laser Exposure for Setting Exchange Bias in Spin Valve Sensors," *Physics Procedia* **75**, 1192–1197 (2015).
- ¹⁷O. Ueberschär, M. J. Almeida, P. Matthes, M. Müller, R. Ecke, R. Ruckriem, J. Schuster, H. Exner, and S. E. Schulz, "Optimized Monolithic 2-D Spin-Valve Sensor for High-Sensitivity Compass Applications," *IEEE Transactions on Magnetics* **51**, 1–4 (2015).
- ¹⁸P. Vallobra, T. Fache, Y. Xu, L. Zhang, G. Malinowski, M. Hehn, J.-C. Rojas-Sánchez, E. E. Fullerton, and S. Mangin, "Manipulating exchange bias using all-optical helicity-dependent switching," *Physical Review B* **96**, 144403 (2017).

- ¹⁹Z. Guo, J. Wang, G. Malinowski, B. Zhang, W. Zhang, H. Wang, C. Lyu, Y. Peng, P. Vallobra, Y. Xu, Y. Xu, S. Jenkins, R. W. Chantrell, R. F. L. Evans, S. Mangin, W. Zhao, and M. Hehn, “Single-Shot Laser-Induced Switching of an Exchange Biased Antiferromagnet,” *Advanced Materials* **36** (2024), 10.1002/adma.202311643, arXiv:2302.04510.
- ²⁰F. J. F. van Riel, S. M. Verduyze, B. Koopmans, and D. C. Leitao, “Understanding field-free single-shot laser-induced reversal of exchange bias,” *Communications Materials* **6**, 110 (2025).
- ²¹G. Vallejo-Fernandez, N. P. Aley, L. E. Fernandez-Outon, and K. O’Grady, “Control of the setting process in CoFe/IrMn exchange bias systems,” *Journal of Applied Physics* **104**, 033906 (2008).
- ²²H. Kanso, R. Patte, V. Baltz, and D. Ledue, “Influence of finite-size and edge effects on the exchange-bias properties of ferromagnetic/antiferromagnetic nanodots: Granular Monte Carlo investigation,” *Physical Review B* **99**, 054410 (2019).
- ²³R. Khantawi, W. Daeng-am, P. Chureemart, R. W. Chantrell, and J. Chureemart, “Exchange bias model including setting process: Investigation of antiferromagnetic alignment fraction due to thermal activation,” *Journal of Applied Physics* **133**, 023903 (2023).
- ²⁴S. Jenkins, R. W. Chantrell, and R. F. L. Evans, “Atomistic simulations of the magnetic properties of $\text{Ir}_x\text{Mn}_{1-x}$ alloys,” *Physical Review Materials* **5**, 034406 (2021).
- ²⁵A. Migliorini, B. Kuerbanjiang, T. Huminiuc, D. Kepaptsoglou, M. Muñoz, J. L. F. Cuñado, J. Camarero, C. Aroca, G. Vallejo-Fernández, V. K. Lazarov, and J. L. Prieto, “Spontaneous exchange bias formation driven by a structural phase transition in the antiferromagnetic material,” *Nature Materials* **17**, 28–35 (2018).
- ²⁶B. Koopmans, G. Malinowski, F. Dalla Longa, D. Steiauf, M. Fähnle, T. Roth, M. Cinchetti, and M. Aeschlimann, “Explaining the paradoxical diversity of ultrafast laser-induced demagnetization,” *Nature Materials* **9**, 259–265 (2010).
- ²⁷M. Beens, M. L. M. Lalieu, A. J. M. Deenen, R. A. Duine, and B. Koopmans, “Comparing all-optical switching in synthetic-ferrimagnetic multilayers and alloys,” *Physical Review B* **100**, 220409 (2019), arXiv:1908.07292.
- ²⁸J. M. D. Coey, *Magnetism and Magnetic Materials* (Cambridge University Press, 2001).
- ²⁹A. P. Malozemoff, “Random-field model of exchange anisotropy at rough ferromagnetic-antiferromagnetic interfaces,” *Physical Review B* **35**, 3679–3682 (1987).
- ³⁰H. Uyama, Y. Otani, K. Fukamichi, O. Kitakami, Y. Shimada, and J.-i. Echigoya, “Effect of antiferromagnetic grain size on exchange-coupling field of Cr70Al30/Fe19Ni81 bilayers,” *Applied Physics Letters* **71**, 1258–1260 (1997).
- ³¹H. N. Fuke, K. Saito, M. Yoshikawa, H. Iwasaki, and M. Sashashi, “Influence of crystal structure and oxygen content on exchange-coupling properties of IrMn/CoFe spin-valve films,” *Applied Physics Letters* **75**, 3680–3682 (1999).
- ³²E. Fulcomer and S. H. Charap, “Thermal fluctuation aftereffect model for some systems with ferromagnetic-antiferromagnetic coupling,” *Journal of Applied Physics* **43**, 4190–4199 (1972).
- ³³K. Nishioka, C. Hou, H. Fujiwara, and R. D. Metzger, “Grain size effect on ferro-antiferromagnetic coupling of NiFe/FeMn systems,” *Journal of Applied Physics* **80**, 4528–4533 (1996).
- ³⁴G. Vallejo-Fernandez, L. E. Fernandez-Outon, and K. O’Grady, “Measurement of the anisotropy constant of antiferromagnets in metallic polycrystalline exchange biased systems,” *Applied Physics Letters* **91** (2007), 10.1063/1.2817230.
- ³⁵R. Y. Umetsu, A. Sakuma, and K. Fukamichi, “Magnetic anisotropy energy of antiferromagnetic L1-type equiatomic Mn alloys,” *Applied Physics Letters* **89** (2006), 10.1063/1.2236103.
- ³⁶M. Meinert, B. Büker, D. Graulich, and M. Dunz, “Large exchange bias in polycrystalline MnN/CoFe bilayers at room temperature,” *Physical Review B* **92**, 144408 (2015).
- ³⁷M. Ali, C. H. Marrows, and B. J. Hickey, “Controlled enhancement or suppression of exchange biasing using impurity δ layers,” *Physical Review B* **77**, 134401 (2008).
- ³⁸D. Polley, J. Chatterjee, H. Jang, and J. Bokor, “Analysis of ultrafast magnetization switching dynamics in exchange-coupled ferromagnet-ferrimagnet heterostructures,” *Journal of Magnetism and Magnetic Materials* **574**, 170680 (2023).

Supplementary Section 1: Dependence of exchange bias coupling on grain area

To simulate the grain area dependence in more detail, we adapted the exchange bias coupling parameter $\mathcal{J}_{\text{ex},0}$ so that it scales with the grain area according to $\mathcal{J}_{\text{ex},0} = \mathcal{J}_{\text{ex,avg}} \sqrt{A_0/A}^{29-31}$. In order to maintain consistency with experimentally observed values, we use a proportionality constant which makes the average value of $\mathcal{J}_{\text{ex},0}$ for our choice of grain size distribution equal to the measured value of $\mathcal{J}_{\text{ex,avg}} = 0.19 \text{ mJ m}^{-2}$ reported in literature²⁸. If we enforce this condition the value of A_0 is fixed according to

$$\begin{aligned} \mathcal{J}_{\text{ex,avg}} &= \frac{\int d\mathbb{L} \mathcal{J}_{\text{ex},0} A}{\int d\mathbb{L} A} \\ \Rightarrow A_0 &= \mu \exp\left(\frac{3}{4}\sigma^2\right). \end{aligned} \quad (\text{S1})$$

For the values of μ and σ used in the main paper this value becomes $A_0 = 50.6 \text{ nm}^2$.

Supplementary Section 2: Parameter spaces of exchange bias magnitude

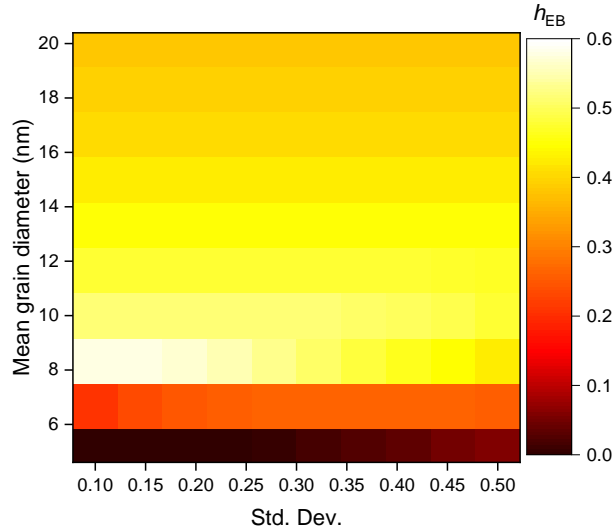


FIG. S1. The value of h_{EB} integrated over all grain areas 1 ms after laser excitation for different combinations of median grain diameter and standard deviation. The modeling results in the paper use a median diameter of 8 nm with a standard deviation of 0.4.

We simulated the effects of different grain size distributions in the antiferromagnetic layer on the reversed exchange bias h_{EB} . The results for a 5 nm thick layer are shown in Fig. S1. A clear optimum can be seen in the grain diameter around 8 nm, which is already a typical value found in polycrystalline IrMn layers²³. However, reducing the standard deviation of the distribution around this optimum does result in an increased h_{EB} value, getting very close to the thermal equilibrium value at room temperature of 0.77. Thus, attempting to reduce the width of the distribution may lead to increased performance for ultrafast laser-induced exchange bias reversal.

Supplementary Section 3: Comparing the model to switching of IrMn/GdCo from literature

Here, we attempt to reproduce the fluence dependence of exchange bias reversal in GdCo alloys as used in the experiments from Guo et al.¹⁹ and plotted in Fig. S2a. We model their stack as a $\text{Gd}_{23}\text{Co}_{77}$ alloy adjacent to 4 IrMn

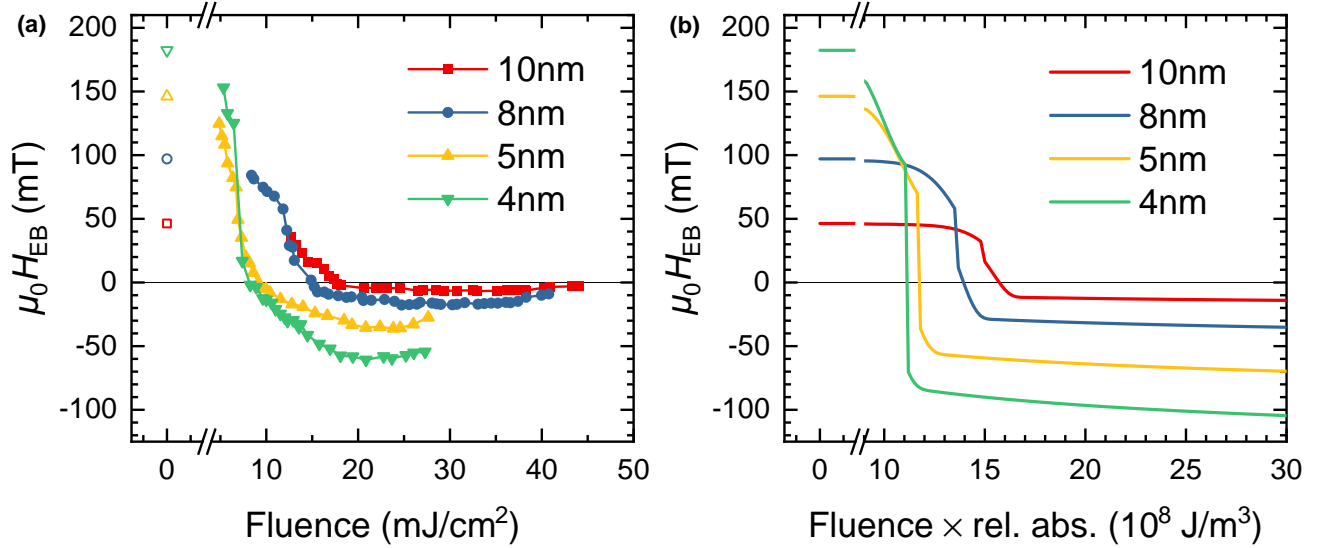


FIG. S2. (a) Experimental results from Guo et al.¹⁹ of exchange bias magnitude after excitation with a femtosecond laser pulse with varying fluences. The sample consists of a 4 nm thick $\text{Gd}_{0.23}\text{Co}_{0.77}$ ferrimagnet on top of a IrMn layer with thicknesses of 4, 5, 8 and 10 nm. (b) Simulation results of the model from the main paper, with the value of h_{EB} scaled according to the values at zero fluence from (a) and with the fluence scaled according to the absorption in the IrMn layer relative to the 10 nm thick IrMn, as calculated by the transfer matrix method.

layers as was done in the main paper. The coordination matrix of this stack is given by

$$\mathbf{C} = \begin{pmatrix} 12x & 12(1-x) & 0 & 0 & 0 & 0 \\ 12x & 12(1-x) & 0 & 0 & 0 & 0 \\ 3x & 3(1-x) & 6 & 3 & 0 & 0 \\ 0 & 0 & 3 & 6 & 3 & 0 \\ 0 & 0 & 0 & 3 & 6 & 3 \\ 0 & 0 & 0 & 0 & 3 & 6 \end{pmatrix}, \quad (\text{S1})$$

where $x = 0.23$ is the Gd-content of the $\text{Gd}_x\text{Co}_{1-x}$ alloy. The value for H_{EB} at zero fluence in Fig. S2a is used as the value for $H_{EB,\text{max}}$ to scale the normalized value of h_{EB} with. Using these parameters produces the fluence dependence in Fig. S2b, which shows excellent qualitative correspondence with the experimental data in Fig. S2a. Most notably, it can be seen that the annealed plateau is not present because the switching threshold overlaps with the fluence where T exceeds T_N , resulting in a sharp jump overlapping the gradual transition of h_{EB} from positive to negative for increasing fluence. Very similar sharp jumps can be identified in Fig. S2a as well.

In addition, the following small adjustments have been made to the model. We set $\mathcal{J}_{\text{Gd,IrMn}} = 0$ to reflect the negligible coupling between Gd and IrMn compared to between Co and IrMn³⁷. Furthermore, we set $\mathcal{J}_{\text{ex},0} = (1-x) \cdot 0.19 \text{ mJ m}^{-2}$ to reflect this difference in coupling strength in the exchange bias as well. Finally, we adjust the fluence parameter to the free-space fluence by calculating the absorption in the IrMn layer for various antiferromagnetic thicknesses via the transfer matrix method (see Ref. 20 and Ref. 38 for details on refractive indices for the individual layers). Normalizing against the absorption in the 10 nm thick layer, this leads to the correction factors 0.75, 0.79 and 0.91 for IrMn thicknesses 4, 5 and 8 nm, respectively. So for example, a 4 nm thick IrMn layer only needs 75% of the free-space fluence compared to a 10 nm thick layer to achieve the same deposited energy per volume. Moreover, the absorption in the GdCo layer is better than in the IrMn layer by about a factor 1.5. Therefore we chose a threshold fluence of $15 \times 10^8 \text{ J m}^{-3}$ for switching the GdCo magnetization, which is slightly lower than the threshold fluence predicted by the M3TM ($34 \times 10^8 \text{ J m}^{-3}$) but which does best match the experimental results from Guo et al.¹⁹. In reality other parameters like τ_D will also inevitably be influenced by the thickness of IrMn, but it would be too cumbersome to attempt implementing all of them. Instead, correcting for the difference in absorption is expected to be enough for capturing most of the effect from varying the IrMn thickness.